symmetry

MDPI

Article

Novel "Anti-Zeolite" $Ba_3Sr_3B_4O_{12}$: Eu^{3+} Phosphors: Crystal Structure, Optical Properties, and Photoluminescence

Rimma S. Bubnova [1,*], Andrey P. Shablinskii [1], Alexey V. Povolotskiy [2], Olga Yu. Shorets [1], Valery L. Ugolkov [1], Sergey N. Volkov [1,3], Valentina A. Yukhno [1] and Stanislav K. Filatov [4]

[1] Institute of Silicate Chemistry of the Russian Academy of Sciences (ISC RAS), Makarova Emb. 2, Saint Petersburg 199034, Russia; shablinskii.andrey@mail.ru (A.P.S.); olga_frooze@rambler.ru (O.Y.S.); ugolkov.52@mail.ru (V.L.U.); s.n.volkov@inbox.ru (S.N.V.); yukhno.valentina@gmail.com (V.A.Y.)
[2] Institute of Chemistry, St. Petersburg State University, Universitetskaya Emb. 7/9, Saint Petersburg 199034, Russia; apov@inbox.ru
[3] Laboratory of Arctic Mineralogy and Material Sciences, Kola Science Centre, Russian Academy of Sciences, Fersmana St. 14, Apatity 184209, Russia
[4] Institute of Earth Sciences, St. Petersburg State University, Universitetskaya Emb. 7/9, Saint Petersburg 199034, Russia; filatov.stanislav@gmail.com
* Correspondence: rimma_bubnova@mail.ru

Abstract: Novel $Ba_3Sr_3B_4O_{12}$: Eu^{3+} phosphors were synthesized by crystallization from a melt. The crystal structures of $Ba_3(Sr_{3-1.5x}Eu_x)B_4O_{12}$ (x = 0.03, 0.06, 0.15, 0.20, 0.25) solid solutions were refined from SCXRD data. The crystal structures of $Ba_3(Sr_{3-1.5x}Eu_x)B_4O_{12}$ phosphors can be described in terms of the cationic sublattice and belong to the "anti-zeolite" family of borates. Its cationic framework is constructed of Ba and Sr atoms. The Eu^{3+} ions occupy the Sr(1) extraframework cationic site in the $Ba_3(Sr_{3-1.5x}Eu_x)B_4O_{12}$ (x = 0.01–0.20) phosphors. The $Ba_3Sr_{2.625}Eu_{0.25}B_4O_{12}$ borate crystallizes in a new structure type ($I4/mcm$, a = 13.132(3), c = 14.633(4) Å, V = 2523.5(11) Å^3, Z = 8, R_1 = 0.067). In the $Ba_3Sr_{2.625}Eu_{0.25}B_4O_{12}$ crystal structure, the Eu^{3+} ions occupy Sr(1) and Ba/Sr(1) sites, which leads to changes in the crystal structure. The Wyckoff letter and occupancy of the O(5) site are changed; B–O anion groups contain two BO_3 triangles (B(3) and B(4)), orientationally disordered over the four orientations, and two ordered BO_3 triangles (B(1) and B(2)) in contrast to $Ba_3Sr_3B_4O_{12}$, in which these groups are disordered over the 4 and 8 orientations. The emission spectra of $Ba_3Sr_3B_4O_{12}$: Eu^{3+} show characteristic lines corresponding to the intraconfigurational 4f-4f transitions of Eu^{3+} ions. $Ba_3Sr_{2.7}Eu_{0.20}B_4O_{12}$ demonstrates the strongest luminescent intensity among $Ba_3(Sr_{3-1.5x}Eu_x)B_4O_{12}$ solid solutions. The increase in the Eu^{3+} content results in a gradual change in chromaticity from light red to orange-red/red. It can be concluded that $Ba_3Sr_3B_4O_{12}$: Eu^{3+} is a promising red phosphor.

Keywords: borate; crystal structure; "anti-zeolite"; phosphors; luminescence; europium-activated phosphor

Citation: Bubnova, R.S.; Shablinskii, A.P.; Povolotskiy, A.V.; Shorets, O.Y.; Ugolkov, V.L.; Volkov, S.N.; Yukhno, V.A.; Filatov, S.K. Novel "Anti-Zeolite" $Ba_3Sr_3B_4O_{12}$: Eu^{3+} Phosphors: Crystal Structure, Optical Properties, and Photoluminescence. *Symmetry* **2023**, *15*, 1399. https://doi.org/10.3390/sym15071399

Academic Editor: Christophe Humbert

Received: 16 June 2023
Revised: 1 July 2023
Accepted: 7 July 2023
Published: 11 July 2023

1. Introduction

A combination of rich crystal chemistry [1–6] and excellent optical properties makes borates important prospective materials [7,8]. Alkaline earth and rare-earth borates also attract great interest as NLO and luminescent materials for different applications [9–11]. The investigations of new borate matrices, which include rare-earth ions, make it possible to create new phosphors and laser materials due to isomorphic substitution. The rare-earth ions most often replace the alkaline earth atoms that are close in ionic radius and coordination number. Recently, it was shown that Eu^{3+}-containing matrices have some advantages, especially for crystal structures with a few independent sites for alkaline earth and rare-earth metals [12–19].

This work is aimed at searching for new matrices for red-emitting phosphors in the SrO–BaO–B_2O_3 system. In the phase relations study of the BaB_2O_4–SrO section of the ternary system, a compound with the preliminary formula $Ba_5Sr_6B_{10}O_{26}$ was discovered, but its diffraction pattern was not indexed [20]. Limited $Ba_{1-x}Sr_xB_2O_4$ solid solutions in a eutectic system based on SrB_2O_4 and BaB_2O_4 compounds were investigated [20]. The crystal structure of $Ba_{1-x}Sr_xB_2O_4$ with x = 1.16 was refined in [21]; it turned out to be similar to α-BaB_2O_4. The $Ba_{0.87}Sr_{3.13}B_{14}O_{25}$ solid solution was refined in [22]. Later, the $Ba_2Sr_3B_4O_{11}$ crystal structure was resolved instead of $Ba_5Sr_6B_{10}O_{26}$ [23], and the $Ba_2Sr_3B_4O_{11}$ borate is structurally similar to $Ba_5B_4O_{11}$ borates [24]. In 2018, the crystal structure of $Ba_3(BO_3)_2$ was resolved in a novel structure type that can be described as "anti-zeolite" with the structural formula $[Ba_{12}(BO_3)_6](BO_3)_2$ [25]. Finally, the disordered $Ba_3Sr_3B_4O_{12}$ borate was obtained for the first time and its crystal structure was similar to the "anti-zeolite" structural family [23]. The $Ba_3Sr_3B_4O_{12}$ crystal structure ($I4/mcm$, a = 13.102(3), c = 14.644(4) Å, V = 2514 (1) $Å^3$) consists of isolated BO_3 radicals oriented in a non-parallel manner. It contains BO_3 triangles orientationally disordered over the 4 and 8 orientations.

The "Anti-zeolite" borate family contains many compounds which crystallize in different space groups; $Ba_6B_4O_{12}$ [25], $Ba_{12}(BO_3)_6(BO_3)_{2-2x}[F_2]_x[F_4]_x$ [26], $Ba_{12}(BO_3)_6(BO_3)_{2-2x}[F_2]_x[F_4]_x$:Cu [27] were described in *Pbam*, while $Ba_{12}(BO_3)_6(BO_3)[LiF_4]$ and $Ba_{12}(BO_3)_6(BO_3)[NaF_4]$ [28] were described in the $P4_2bc$ space group. $Ba_{12}(BO_3)_6(BO_3)_{2-2x}[MnF_6]_x$ [29] and $Nd_xBa_{12}(BO_3)_{8-x}F_{6x}$ [30] belong to the $I4/mcm$ space group.

In this study, the novel red-emitting $Ba_3Sr_3B_4O_{12}$: Eu^{3+} phosphor was synthesized by cooling from a melt. There are three independent sites in $Ba_3Sr_3B_4O_{12}$ borate for Ba and Sr cations, in which Ba and Sr atoms are partially ordered [23]: Sr(1), Ba(1), and Sr/Ba(1). A comparison of the cations I_r and the average bond lengths of the $Ba(1)O_8$, $Sr(1)O_7$, and $Sr/Ba(1)O_{11}$ gave us the expectation that Sr(1) is the preferable crystallographic site for Eu^{3+} incorporation. The crystal structure of $Ba_3(Sr_{3-1.5x}Eu_x)B_4O_{12}$ (x = 0.03, 0.06, 0.15, 0.20, 0.25) solid solutions and distribution of the Eu^{3+} ions over cation sites were refined, and luminescent and optical properties were investigated.

2. Materials and Methods

The $Ba_3(Sr_{3-1.5x}Eu_x)B_4O_{12}$ (x = 0.01, 0.03, 0.06, 0.15, 0.20, 0.25) phosphors were synthesized by mixing $BaCO_3$ (Reahim, 99.99% purity), H_3BO_3 (Neva Reaktiv, 99.90% purity), $SrCO_3$ (Reahim, 99.99% purity), and Eu_2O_3 (Kyrgyz CMC, 99.93% purity) in their stoichiometric ratios. The pellets of the reactant mixtures were heated in platinum crucibles at 900 °C for 20 h and at 1000 °C for 12 h. After that, the samples were melted at 1400 °C and cooled to room temperature over 7 h.

The samples were characterized by powder X-ray diffraction using a Rigaku Smart SE diffractometer (CuKα, 2θ = 3–120°, step 0.02). The phase composition was determined using the PDF-2 (ICDD) database. X-ray phase analysis revealed that the polycrystalline samples of $Ba_3(Sr_{3-1.5x}Eu_x)B_4O_{12}$ (x = 0.01, 0.03, 0.06, 0.12, 0.15, 0.20, 0.25) were homogenous.

Single crystals of $Ba_3(Sr_{3-1.5x}Eu_x)B_4O_{12}$ (x = 0.03, 0.06, 0.15, 0.20, 0.25) phosphors were selected using an optical microscope in polarized light from polycrystalline aggregates and then attached to the end of glass fiber using an epoxy glue. The experimental data were collected on a Rigaku XtaLab Synergy-S diffractometer equipped with high-speed direct-action detector HyPix-6000HE. A hemisphere of three-dimensional data was collected using MoKα radiation and frame width of 1° in ω, with 25 s used to acquire each frame. The data were interpolated into the CrysAlisPro software (2015) for further processing. An absorption correction was introduced using the SCALE3 ABSPACK algorithm. The crystal structures were refined with the JANA2006 program package [31]. The main details of the X-ray diffraction experiment and selected bond lengths are summarized in Tables 1 and 2. Final atomic coordinates and displacement parameters are given in Tables S1–S10. Occupancies of the cation sites were refined from the experimental site-scattering factors in accordance with the chemical composition (Table S11). Strontium

scattering curves were used to refine site occupancy. The criteria for occupancy assignment are scattering power, coordination number, and average bond lengths. Further details of the crystal structure investigations can be obtained from the Cambridge Structural Database on quoting the depository numbers CSD 2269856, 2269867, 2269885, 2269886, and 2269887.

Table 1. Crystal data, data collection, and details of refinement of the $Ba_3(Sr_{3-1.5x}Eu_x)B_4O_{12}$ phosphors.

Eu_x	**0.03**	**0.06**	**0.15**	**0.20**	**0.25**
M_r	910.7	911.3	913.2	914.2	915.4
Crystal system, space group	Tetragonal, *I*4/*mcm*				
Temperature (°C)	25				
a, Å	13.163 (3)	13.154 (3)	13.167 (3)	13.151 (3)	13.132 (3)
c, Å	14.608 (4)	14.612 (4)	14.634 (4)	14.653 (4)	14.633 (4)
V, Å^3	2531.1 (11)	2528.3 (11)	2537.0 (11)	2534.5 (11)	2523.5 (11)
Z	8				
Radiation type	Mo *K*α				
μ (mm^{-1})	21.76	21.74	21.54	21.49	21.52
Crystal size (mm)	0.08 × 0.13 × 0.15	0.07 × 0.12 × 0.13	0.10 × 0.12 × 0.14	0.10 × 0.09 × 0.15	0.11 × 0.13 × 0.17
Diffractometer	Rigaku XtaLab Synergy-S				
No. of measured, independent, and observed [$I > 3\sigma(I)$] reflections	24,289, 786, 533	26,613, 807, 512	27,486, 808, 615	24,411, 633, 451	9670, 776, 270
R_{int}	0.145	0.116	0.112	0.174	0.148
$(\sin\theta/\lambda)_{max}$ (Å^{-1})	0.781	0.777	0.776	0.777	0.777
R (obs), *wR*(obs), *S*	0.070, 0.070, 2.20	0.051, 0.059, 1.83	0.051, 0.069, 2.89	0.058, 0.069, 2.42	0.068, 0.093, 1.02
No. of reflections	787	807	808	633	776
No. of parameters	64	65	64	64	56
No. of restraints	3	2	2	2	4

Table 2. Selected bond length (Å) in the $Ba_3(Sr_{3-1.5x}Eu_x)B_4O_{12}$ structure.

x	**0.03**	**0.06**	**0.15**	**0.2**	**0.25**
Ba(1)–O(2) × 2	2.640 (12)	2.616 (9)	2.645 (9)	2.671 (13)	2.665 (15)
Ba(1)–O(1) × 4	2.791 (10)	2.814 (7)	2.814 (7)	2.816 (10)	2.822 (15)
<Ba(1)–O>$_6$	2.74	2.75	2.76	2.77	2.77
Ba(1)–O(2)	3.271(14) × 2	3.266(11) × 2	3.295 (10) × 2	3.270 (15) × 2	3.277(18) × 2
<Ba(1)–O>$_8$	2.87	2.88	2.89	2.89	2.90
Sr(1)–O(4)	2.435 (10)	2.428 (10)	2.460 (11)	2.484 (16)	2.511 (18)
Sr(1)–O(1) × 2	2.595 (15)	2.586 (10)	2.588 (11)	2.586 (15)	2.541 (16)
Sr(1)–O(3) × 4	2.686 (14)	2.655 (10)	2.641 (10)	2.660 (15)	2.669 (16)
<Sr(1)–O>$_7$	2.62	2.60	2.60	2.61	2.61
Sr/Ba(1)–O(5)	2.42 (5)	2.33 (4)	2.45 (3)	2.42 (5)	2.297 (11)
Sr/Ba(1)–O(5)	2.49 (4)	2.56 (4)	2.51 (4)	2.60 (6)	3.167 (4)
Sr/Ba(1)–O(5)	2.57 (5)	2.57 (3)	2.50 (4)	2.48 (6)	-
Sr/Ba(1)–O(3)	2.616 (13)	2.604 (9)	2.608 (10)	2.593 (14)	2.627 (16)
Sr/Ba(1)–O(2)	2.641 (12)	2.641 (9)	2.628 (9)	2.635 (13)	2.631 (15)
Sr/Ba(1)–O(3)	2.710 (15)	2.740 (11)	2.713 (12)	2.738 (16)	2.690 (16)
Sr/Ba(1)–O(6)	2.84 (2)	2.908 (18)	2.88 (2)	2.88 (3)	2.62 (4)
Sr/Ba(1)–O(1)	2.854 (10)	2.828 (7)	2.829 (7)	2.826 (10)	2.821 (15)
Sr/Ba(1)–O(6)	2.86 (3)	2.771 (17)	2.81 (2)	2.83 (3)	2.62 (4)
Sr/Ba(1)–O(4)	2.901 (10)	2.897 (8)	2.897 (8)	2.889 (11)	2.892 (14)
Sr/Ba(1)–O(3)	3.083 (14)	3.117 (11)	3.142 (11)	3.133 (15)	3.115 (17)
<Sr/Ba(1)–O>$_{11}$	2.73	2.72	2.72	2.73	2.75 *

Table 2. *Cont.*

x	0.03	0.06	0.15	0.2	0.25
B(1)–O(2) B(1)–O(3) × 2	1.36 (3) 1.37 (3)	1.37 (2) 1.37 (2)	1.363 (18) 1.394 (17)	1.30 (4) 1.39 (3)	1.37 (4) 1.35 (4)
<B(1)–O>$_3$	1.36	1.37	1.383	1.36	1.36
B(2)–O(1) × 2 B(2)–O(4)	1.39 (2) 1.30 (2)	1.36 (4) 1.38 (5)	1.36 (2) 1.35 (2)	1.33 (3) 1.38 (3)	1.36 (3) 1.36 (3)
<B(2)–O>$_3$	1.36	1.37	1.36	1.35	1.36
B(4)–O(6) × 4	1.40 (3)	1.45 (2)	1.42 (2)	1.41 (3)	1.51 (5)
<B(4)–O>$_4$	1.40	1.45	1.42	1.41	1.51
B(3)–O(5)	1.37 (3) × 8	1.41 (3) × 8	1.41 (3) × 8	1.39 (4) × 8	1.40 (2) × 4
<B(3)–O>$_8$	1.37	1.41	1.41	1.39	1.40 **

* <Sr/Ba(1)–O>$_{10}$. ** <B(3)–O>$_4$.

The absorption spectra were measured with a Lambda 1050 (Perkin Elmer) spectrometer. To avoid the influence of light scattering, measurements were carried out in the 150 mm integrating sphere. Photoluminescence (PL) and photoluminescence excitation (PLE) spectra and emission kinetic curves were measured on a Fluorolog-3 spectrometer (Horiba Jobin Yvon, Darmstadt, Germany). To study the luminescent properties, polycrystalline powders were pressed into KBr tablets. The vibrational spectra were obtained with a LabRam HR800 spectrometer (Horiba Jobin Yvon).

The DSC studies of $Ba_3(Sr_{3-1.5x}Eu_x)B_4O_{12}$ (x = 0.03, 0.15, 0.25) solid solutions were performed on NETZSCH STA 429 with the use of a standard sample holder for measuring the differential scanning calorimetry (DSC)/differential thermal analysis (DTA) and thermogravimetry (TG) curves. The samples in the form of tablets were placed in a platinum crucible and heated up to 1500 °C in air at a rate of 20 °C/min. The sample weight was about 30 mg. The temperatures of the thermal effects were estimated as onset temperatures. According to the TG data, very small mass losses gradually occurred during heating, apparently due to the high heating rate.

3. Results and Discussion

3.1. Powder X-ray Diffraction of the $Ba_3(Sr_{3-1.5x}Eu_x)B_4O_{12}$ (x = 0.01, 0.03, 0.06, 0.12, 0.15, 0.20, 0.25) Phosphors

Powder XRD patterns for all studied samples are shown in Figure 1. The samples are homogeneous and peaks correspond to the calculated XRD patterns of $Ba_3(Sr_{3-1.5x}Eu_x)B_4O_{12}$ borates in accordance with data [23]. Unit cell parameters were refined by the Rietveld method in the RTT program software (v.2). The a parameter is decreased with the increase in Eu content as well as the volume V of the $Ba_3(Sr_{3-1.5x}Eu_x)B_4O_{12}$ phosphors, due to the difference in the ionic radii of the Sr ($^{[7]}$1.35 Å) and Eu ($^{[7]}$1.15 Å) ions [32] (Figure 2), while the c parameter is increased slightly to about x = 0.10–0.15 Eu^{3+}, but practically does not increase further. It could be assumed that the inflection point may be caused by a partial redistribution of Eu ions over Sr(1) and Sr/Ba(1) sites, as occurred in $Ba_3Lu_2B_6O_{15}$ [19].

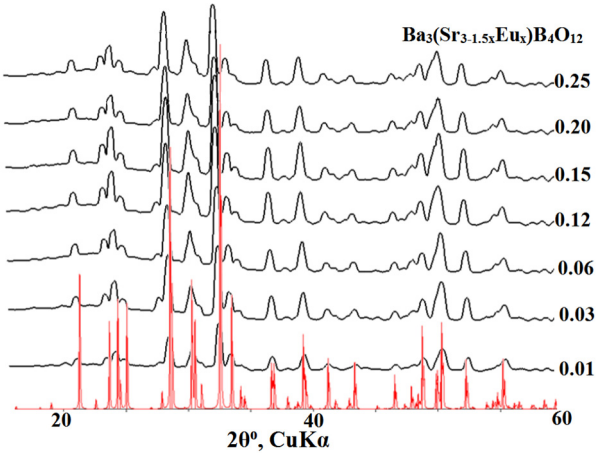

Figure 1. Powder X-ray diffraction patterns of the $Ba_3(Sr_{3-1.5x}Eu_x)B_4O_{12}$ phosphors. Red lines mark the calculated powder XRD pattern of $Ba_3Sr_3(BO_3)_4$.

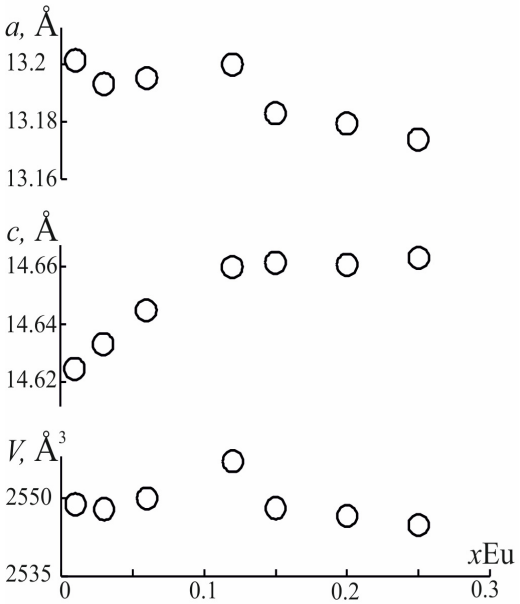

Figure 2. Dependence of unit cell parameters vs. europium concentration $x(Eu^{3+})$ in the $Ba_3(Sr_{3-1.5x}Eu_x)B_4O_{12}$ phosphors.

3.2. Thermal Analysis

DSC curve of the $x = 0.03$ solid solution demonstrates small thermal effects on heating at 1194 and 1262 °C and a strong effect at 1305 °C (Figure 3a). The thermal effects at 1194 and 1305 °C refer to solidus and liquidus temperatures; these effects agree with data for $Ba_3Sr_3B_4O_{12}$ (1188 and 1343 °C) from [23]. The temperature of the strong effect is lower due to lowering of the liquidus temperature for solid solutions. The intermediate small thermal effect at 1262 °C may be caused by the recrystallization of solid solutions during their melting. The melting process of solid solutions occurs via the two-phase (solid and liquid) region, in which the chemical compositions of liquid and solid phases are continuously changed from solidus to liquidus temperatures. The $Ba_3B_2O_6$ compound melts congruently at 1390 °C [25]. Therefore, the solidus and liquidus temperatures for disordered $Ba_3Sr_3B_4O_{12}$ and $Ba_3(Sr_{2.965}Eu_{0.03})B_4O_{12}$ solid solutions are significantly lower relative to $Ba_3B_2O_6$.

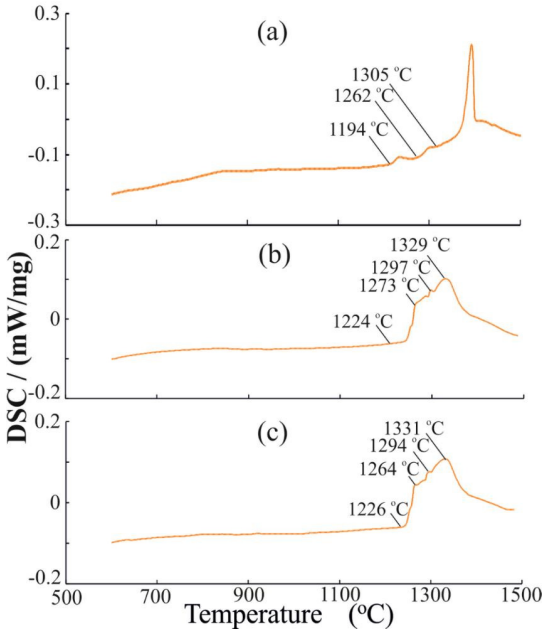

Figure 3. DSC heating curves for (**a**) $Ba_3(Sr_{2.955}Eu_{0.03})B_4O_{12}$, (**b**) $Ba_3(Sr_{2.775}Eu_{0.15})B_4O_{12}$, and (**c**) $Ba_3(Sr_{2.625}Eu_{0.25})B_4O_{12}$.

DSC heating curves of $x = 0.15$ and $x = 0.25$ samples are very similar (Figure 3b,c), although they differ from the curve with $x = 0.03$. They demonstrate broadened overlapping peaks of solid solutions melting (Figure 3b,c). The thermal effects start at 1224 and 1226 °C for $x = 0.15$ and $x = 0.25$ samples, respectively. Apparently, these peaks (maxima at 1267 and 1264 °C) correspond to solidus temperatures, while the final maxima (1329 and 1331 °C) are liquidus temperatures. Intermediate insignificant peaks are attributed as recrystallization due to reaction of the solid phase and liquid with chemical composition changes for solid and liquid phases. The melting region of solid solutions with a high Eu^{3+} content ($x = 0.15$ and 0.25) is narrower than in the case of $x = 0.03$, which can apparently indicate a change in the structure of the solid solutions.

3.3. Crystal Structure Description

There is one symmetrically independent Ba, one Sr, one Sr/Ba, four B, and six O sites in crystal structures of $Ba_3(Sr_{3-1.5x}Eu_x)B_4O_{12}$ solid solutions. The Ba(1), Sr(1), and Sr/Ba(1) are surrounded by six/eight, seven, and eleven oxygen atoms, respectively.

The crystal structures of $Ba_3(Sr_{3-1.5x}Eu_x)B_4O_{12}$ phosphors, borates with isolated B–O anions, can be described in terms of the cationic sublattice and belong to the "antizeolite" family of borates [25,28,29,33,34]. This structure is formed by a tetragonal cationic framework of Ba and Sr atoms with square, pentagonal, and triangular cavities (Figure 4, bottom) filled by B–O anionic groups, as in $Ba_3B_2O_6$ borate [25]. Each square cavity is surrounded by four pentagonal and triangular ones. This framework can be divided into A and B double pseudolayers [**34**] due to inversion center and mirror plane along the c axis (Figure 4, center). The $[B(1)O_3]$ and $[B(2)O_3]$ triangular radicals are located in pentagonal and triangular cavities inside A pseudolayers. The Sr(1) is an extraframework cationic site which is located within B pseudolayers.

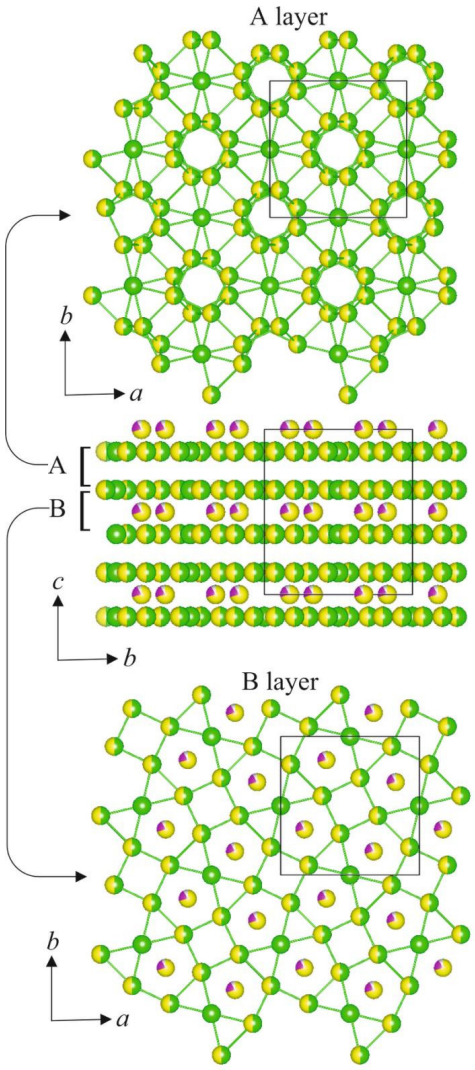

Figure 4. Cationic pseudolayers in the $Ba_3(Sr_{2.70}Eu_{0.20})B_4O_{12}$ crystal structure.

The large channels in the $Ba_3(Sr_{2.70}Eu_{0.20})B_4O_{12}$ crystal structure are formed by square cavities of cationic nets: face-to-face connected "cubes" and anti-cubes (Figure 5, left center) forming a system of channels along the *c* axis. There are $[B(3)O_3]$ and $[B(4)O_3]$ groups in these channels. They are disordered over the 4 and 8 orientations, in contrast to $Ba_3B_2O_6$, in which these groups are disordered over the 4 orientations.

In the $Ba_3(Sr_{3-1.5x}Eu_x)B_4O_{12}$ (x = 0.03–0.20) crystal structures, the Eu^{3+} atoms occupy the Sr(1) extraframework cationic site according to single-crystal X-ray diffraction data. Preferably, Eu^{3+} ions may replace Sr ions, since the ions have similar ionic radii R_{cryst} ($^{[7]}Sr$ = 1.35 and $^{[7]}Eu^{3+}$ = 1.15 Å), in contrast to barium ($^{[7]}Ba$ = 1.52 Å). If the Sr(1) site is occupied by Eu^{3+} ions by more than 20%, then, as the concentration increases, the Eu^{3+} ions begin to occupy the Sr/Ba(1) site. Previously, the solid solutions of the "anti-zeolite" family were obtained by substitution of the disordered BO_3 groups in the square cavity by different anionic groups [26–30]. Therefore, the $Ba_3(Sr_{3-1.5x}Eu_x)B_4O_{12}$ solid solutions are the first examples of extraframework cationic site substitution in the "anti-zeolite" family of borates.

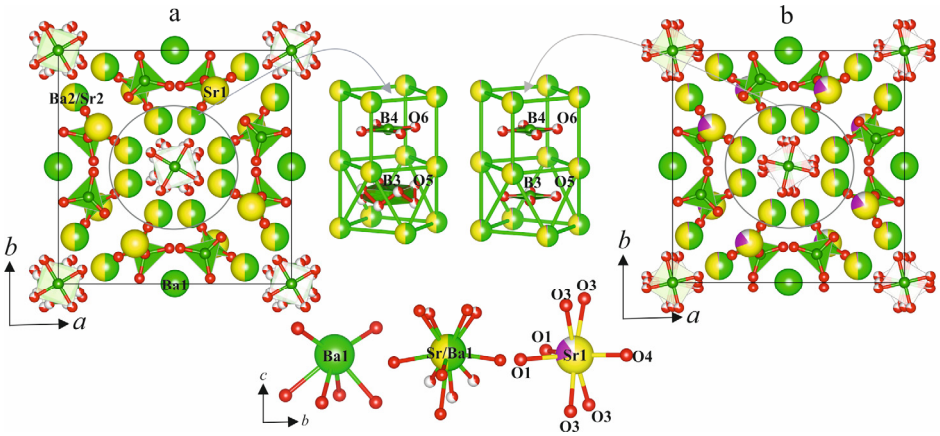

Figure 5. The comparison of $Ba_3Sr_3B_4O_{12}$ (**a**) and $Ba_3Sr_{2.625}Eu_{0.25}B_4O_{12}$ (**b**) crystal structures.

As the Eu content in the Sr(1) site increases, the A pseudolayer thickness (3.4 Å) does not change up to $x = 0.20$ (3.39 Å), while the B pseudolayer thickness, in which Sr(1) cations are located, increases insignificantly from 3.9 to 3.93 Å (Figure 4). When Eu^{3+} ions begin to occupy the Sr/Ba(1) site ($x = 0.25$), thicknesses of A and B pseudolayers (3.39 Å and 3.925 Å) practically do not change, which manifests itself in the appearance of an inflection on the dependence of the *c* parameter vs. Eu content (Figure 2). The equatorial bond lengths of the $Sr(1)O_7$ polyhedra increase for Sr(1)–O(4) from 2.43(1) to 2.51(2) and decrease for Sr(1)–O(1) from 2.595(15) to 2.541(16) Å, respectively. The "apical" bonds of the Sr(1)–O(3) polyhedra decrease insignificantly from 2.686(15) to 2.669(16) (Sr(1)–O(3)) Å (Table 2).

In the $Ba_3Sr_{2.625}Eu_{0.25}B_4O_{12}$ ($x = 0.25$) crystal structure, the Eu^{3+} ions occupy Sr(1) and Sr/Ba(1) sites, which leads to changes in the crystal structure. The Wyckoff letter and occupancy of the O(5) site became 16*j* and 0.75 instead of 32*m* and 0.375 in the $Ba_3(Sr_{3-1.5x}Eu_x)B_4O_{12}$ ($x = 0$–0.20) solid solutions. In the $Ba_3Sr_{2.625}Eu_{0.25}B_4O_{12}$ crystal structure, due to a change in the O(5) site symmetry, the B(4)–O(5) anion group is orientationally disordered over the 4 orientations (Figure 5, right center) instead of 8 orientations (left) in $Ba_3(Sr_{3-1.5x}Eu_x)B_4O_{12}$ ($x = 0$–0.20). The $Ba_3Sr_{2.625}Eu_{0.25}B_4O_{12}$ borate crystallizes in a new structure type ($I4/mcm$, $a = 13.132$, $c = 14.633(4)$ Å, $V = 2523.5$ (11) $Å^3$, $Z = 8$, $R_1 = 0.067$) because the atomic sites are not the same as in the $Ba_3Sr_3B_4O_{12}$ crystal structure, although $Ba_3Sr_{2.625}Eu_{0.25}B_4O_{12}$ and $Ba_3Sr_3B_4O_{12}$ crystallize in the same space group type. The difference between crystal structures is the different configuration of the disordered BO_3 triangles in the channels along the *c* axis (Figure 5). Except for the "anti-zeolite" family, similar coordination of B–O environments has also been found in $Ln_{14}(GeO_4)_2(BO_3)_6O_8$ (Ln = Nd, Sm) [35], $Li_2Rb_7Sr_{24}(BO_3)_{19}$ [36], $Lu_5Ba_6(BO_3)_9$ [37], $Pb_2(BO_3)(NO_3)$ [38], and $Rb_9Ba_{24}(BO_3)_{19}$ [39].

The $3Sr \rightarrow 2Eu + \square$ substitution affects the increase in the size of the square cavity of the channels along the *c* axis. The internal diameter of $Ba_3Sr_3B_4O_{12}$, measured as the distance between the closest cations across the cavity, is 5.57 Å. This value provides a crystallographic free diameter of 4.13 Å, which is similar to those of the small-pore zeolites. A crystallographic free diameter was found by subtracting the averaged ionic radius of Sr and Ba for a coordination number of 7 from the distance between the closest cations across the cavity. The internal diameter and crystallographic free diameter of the channels of $Ba_3(Sr_{3-1.5x}Eu_x)B_4O_{12}$ ($x = 0.20$) are 5.62 and 4.18 Å, respectively. In accordance with these data, we can control the size of the square tubes by substitution of the extrafamework cation sites by different cations.

3.4. Raman Spectroscopy

The Raman spectra of the $Ba_3(Sr_{3-1.5x}Eu_x)B_4O_{12}$ ($x = 0.01$, 0.03, 0.06, 0.12, 0.15, 0.20, 0.25) samples are shown in Figure 6. All Raman bands observed in the spectra around 200, 400, 600, and 900 cm^{-1} correspond to vibrations of BO_3 triangles [40]. No bands

corresponding to BO_4 tetrahedra were found in the Raman spectra, which agrees with structural data. The relatively large width of the Raman bands compared, for example, with $LuBO_3$ single crystal, is explained by the disordered BO_3 triangles in the channels along the *c* axis (Figure 6).

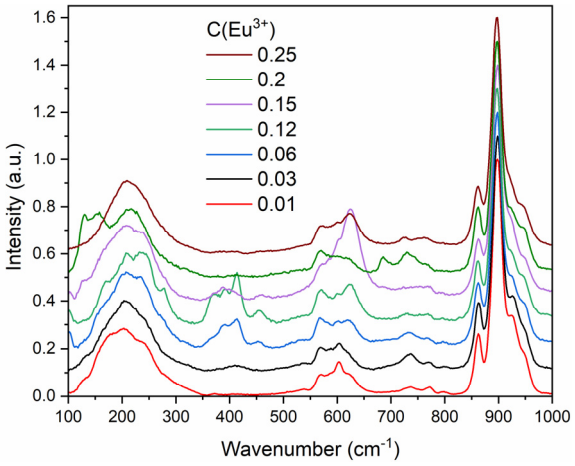

Figure 6. Raman spectra of the $Ba_3Sr_3B_4O_{12}$:Eu^{3+} phosphors.

3.5. Absorption Spectroscopy

The absorption spectra of the $Ba_3(Sr_{3-1.5x}Eu_x)B_4O_{12}$ samples were used to determine the optical band gap in Tauc plot coordinates. Figure 7a shows the example of the Tauc plot for the $x = 0.01$ sample. The dependence of the obtained optical band gap on the Eu^{3+} content is shown in (Figure 7b). Like the data in [34], the absorption edge shift depends on the degree of filling of the cationic framework with anionic clusters. The Sr → Eu substitution of the extraframework site affects the absorption edge shift too (Figure 7b). The band gap of the $Ba_3Sr_3B_4O_{12}$ is 6.10 eV [23] and the band gap for $x = 0.01$ is 3.80 eV. The band gap reduction may be due to the formation of defective localized states in the band gap upon the incorporation of Eu^{3+} ions.

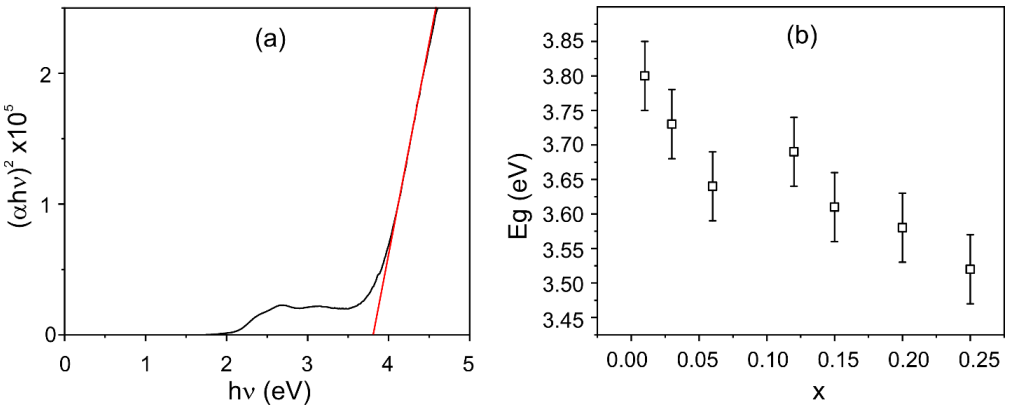

Figure 7. Tauc plot for $Ba_3(Sr_{3-1.5x}Eu_x)B_4O_{12}$ ($x = 0.01$) solid solution (**a**). Dependence of band gap on Eu^{3+} concentration for $Ba_3(Sr_{3-1.5x}Eu_x)B_4O_{12}$ phosphors (**b**).

3.6. Photoluminescence Properties

PLE and PE spectra of $Ba_3Sr_3B_4O_{12}$: Eu^{3+} samples are presented in Figure 8. All narrow bands observed in the spectra correspond to transitions of Eu^{3+} ions. The O^{2-}–Eu^{3+} charge transfer excitation band is observed on PLE spectra below 300 nm. When the photoluminescence of europium is directly excited, the $^7F_0$-$^5L_6$ transition is the most effective (Figure 8a). Therefore, PL spectra were obtained under 392 nm excitation.

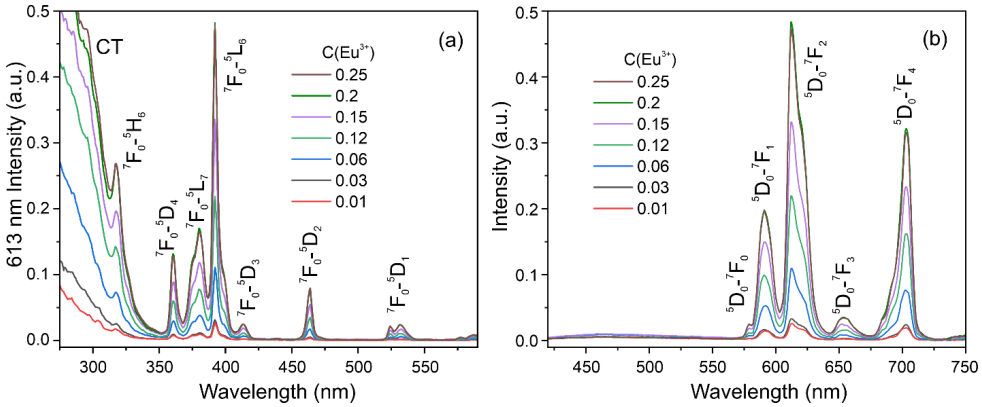

Figure 8. PLE spectra at 613 nm emission (**a**) and PL spectra at 392 nm excitation (**b**) of $Ba_3(Sr_{3-1.5x}Eu_x)B_4O_{12}$ phosphors.

Figure 8b clearly shows that with an increase in the concentration of active ions up to $x = 0.20$, the luminescence intensity increases. At a concentration of $x = 0.25$, the concentration quenching makes a significant contribution and the intensity of the luminescence decreases, as shown in the concentration dependence (Figure 9). If Eu^{3+} ions are distributed over cation sites, then concentration quenching occurs in $Ba_3Sr_3B_4O_{12}$:Eu^{3+} phosphors. Therefore, the main mechanism of concentration quenching is the dipole–dipole interaction between Eu^{3+} ions.

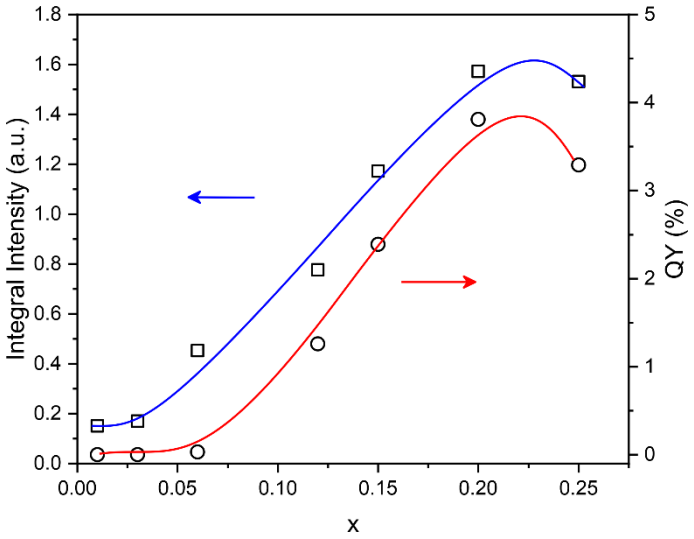

Figure 9. Concentration dependence of the integrated luminescence intensity and PL quantum yield of $Ba_3(Sr_{3-1.5x}Eu_x)B_4O_{12}$ samples.

The lifetimes of the $^5D_0$ level of Eu^{3+} ions were determined from the PL kinetic decay curves for the $^5D_0$-$^7F_2$ transition upon excitation at 392 nm. The concentration dependence of obtained lifetimes is plotted in Figure 10. It can be seen that the $^5D_0$ level lifetime of Eu^{3+} does not depend on the active ion concentration, which indicates the absence of additional channels of excitation or relaxation, such as energy or charge transfer.

The emission spectra were used to determine the chromaticity coordinates, the values of which are presented in Table 3. The Commission Internationale de I'Eclairage (CIE) diagram is presented in Figure 11. It can be seen that the increase in Eu^{3+} concentration leads to a shift in color to the red region.

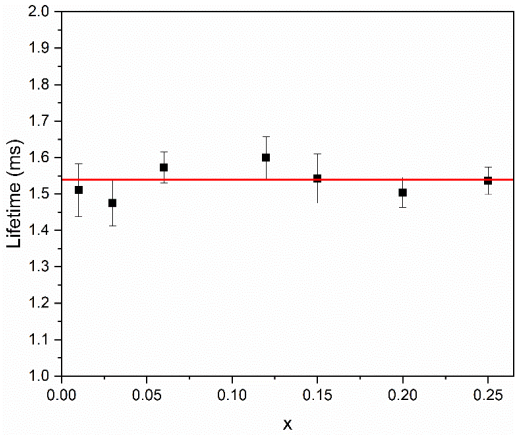

Figure 10. Dependence of Eu^{3+} $^5D_0$ level lifetime on Eu^{3+} concentration.

Table 3. CIE (CIE 1931) chromaticity coordinates of the $Ba_3Sr_3B_4O_{12}$:Eu^{3+} phosphors.

C (Eu^{3+})	*x*	*y*
0.01	0.449	0.319
0.03	0.415	0.310
0.06	0.509	0.330
0.12	0.591	0.343
0.15	0.586	0.342
0.2	0.623	0.346
0.25	0.623	0.346

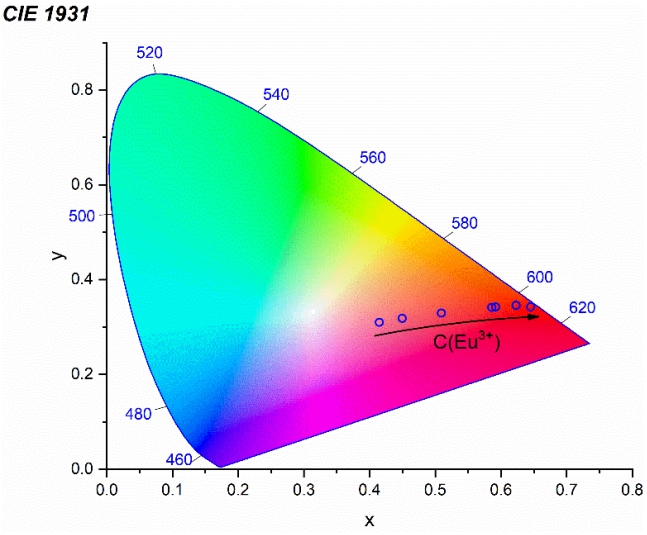

Figure 11. CIE diagram of the $Ba_3(Sr_{3-1.5x}Eu_x)B_4O_{12}$ phosphors.

4. Conclusions

A series of new $Ba_3(Sr_{3-1.5x}Eu_x)B_4O_{12}$ (x = 0.01–0.25) red-emitting phosphors were obtained by crystallization from a melt. The crystal structures of $Ba_3(Sr_{3-1.5x}Eu_x)B_4O_{12}$ (x = 0.03, 0.06, 0.15, 0.20, 0.25) phosphors were solved by the charge flipping method and refined in the tetragonal space group *I*4/*mcm*. The Eu^{3+} ions occupy the Sr(1) extraframework cationic site according to SCXRD data in the $Ba_3(Sr_{3-1.5x}Eu_x)B_4O_{12}$ (x = 0.01–0.20). In the $Ba_3Sr_{2.625}Eu_{0.25}B_4O_{12}$ crystal structure, the Eu^{3+} ions occupy Sr(1) and Sr/Ba(1) sites,

which leads to changes in the crystal structure. The $Ba_3Sr_{2.625}Eu_{0.25}B_4O_{12}$ borate crystallizes in a new structure type ($I4/mcm$, a = 13.132(3), c = 14.633(4) Å, V = 2523.5(11) Å^3, Z = 8, R_1 = 0.067). The Wyckoff letter and occupancy of the O(5) site are changed in the $Ba_3Sr_{2.625}Eu_{0.25}B_4O_{12}$ crystal structure; B–O anion groups contain two BO_3 triangles (B(3) and B(4)), orientationally disordered over the 4 orientations, and two ordered BO_3 triangles (B(1) and B(2)).

Photoluminescence spectra of the $Ba_3Sr_3B_4O_{12}$: Eu^{3+} demonstrate that the characteristic lines correspond to the intra-configurational transitions inside Eu^{3+} ions. The optimal europium doping concentration is x = 0.20. If Eu^{3+} ions are distributed over cation sites, then concentration quenching occurs in $Ba_3Sr_3B_4O_{12}$:Eu^{3+} phosphors. Therefore, the main mechanism of concentration quenching is the dipole–dipole interaction between Eu^{3+} ions. Growth of the Eu^{3+} content leads to the change in CIE color coordinates from light red to red.

Supplementary Materials: The following supporting information can be downloaded at: https://www.mdpi.com/article/10.3390/sym15071399/s1. Table S1: Atomic coordinates, equivalent isotropic displacement parameters (Å^2) and structural occupation factor for x = 0.03; Table S2. Anisotropic atomic displacement parameters (Å^2) for x = 0.03; Table S3. Atomic coordinates, equivalent isotropic displacement parameters (Å^2) and structural occupation factor for x = 0.06; Table S4. Anisotropic atomic displacement parameters (Å^2) for x = 0.06; Table S5. Atomic coordinates, equivalent isotropic displacement parameters (Å^2) and structural occupation factor for x = 0.15; Table S6. Anisotropic atomic displacement parameters (Å^2) for x = 0.15; Table S7. Atomic coordinates, equivalent isotropic displacement parameters (Å^2) and structural occupation factor for x = 0.20; Table S8. Anisotropic atomic displacement parameters (Å^2) for x = 0.20; Table S9. Atomic coordinates, equivalent isotropic displacement parameters (Å^2) and structural occupation factor for x = 0.25; Table S10. Anisotropic atomic displacement parameters (Å^2) for x = 0.25.

Author Contributions: Writing—original draft, R.S.B., A.P.S., O.Y.S. and A.V.P.; Writing—review and editing, A.P.S., O.Y.S., S.K.F. and R.S.B.; Investigation, A.P.S., V.L.U., A.V.P., O.Y.S., S.N.V. and V.A.Y.; Project administration, A.P.S., O.Y.S. and R.S.B.; Data curation, A.P.S., R.S.B. and S.K.F.; Visualization, A.P.S., O.Y.S. and A.V.P.; Supervision, R.S.B. All authors have read and agreed to the published version of the manuscript.

Funding: This work was supported by the Ministry of Science and Higher Education of the Russian Federation within the scientific tasks of the Institute of Silicate chemistry (Russian Academy of Sciences) [project number 0081-2022-0002] (synthesis), and the Russian Science Foundation [grant number 22-23-01133] (data evaluation and generalization, XRD and photoluminescence experiments, investigation of glasses, Raman and Absorption spectroscopy).

Data Availability Statement: Data Availability Statement: CCDC 2269856, 2269867, 2269885, 2269886, and 2269887 contain the crystallographic data for this paper. These data can be obtained free of charge via https://www.ccdc.cam.ac.uk/Community/Depositastructure/CSDCommunications/ (accessed on 25 November 2022).

Acknowledgments: The X-ray diffraction experiments were performed at The Centre for X-ray Diffraction Studies (Saint Petersburg State University). The Raman spectra and luminescence were collected at the Center for Optical and Laser Materials Research, Research Park of Saint Petersburg State University.

Conflicts of Interest: The authors declare no conflict of interest.

References

1. Hawthorne, F.C.; Burns, P.C.; Grice, J.D. The crystal chemistry of boron. *Rev. Miner.* **1996**, *33*, 41–116.
2. Touboul, M.; Penin, N.; Nowogrocki, G. Borates: A survey of main trends concerning crystal-chemistry, polymorphism and dehydration process of alkaline and pseudo-alkaline borates. *Solid State Sci.* **2003**, *5*, 1327–1342. [CrossRef]
3. Yu, D.; Xue, D. Bond analyses of borates from the Inorganic Crystal Structure Database. *Acta Crystallogr.* **2006**, *B62*, 702–709. [CrossRef]
4. Yuan, G.; Xue, D. Crystal chemistry of borates: The classification and algebraic description by topological type of fundamental building blocks. *Acta Crystallogr.* **2007**, *B63*, 353–362. [CrossRef]
5. Bubnova, R.S.; Filatov, S.K. High-temperature borate crystal chemistry. *Z. Kristallogr.* **2013**, *228*, 395–428. [CrossRef]

6. Huang, C.; Mutailipu, M.; Zhang, F.; Griffith, K.J.; Hu, C.; Yang, Z.; Griffin, J.M.; Poeppelmeier, K.R.; Pan, S. Expanding the chemistry of borates with functional $[BO_2]^-$ anions. *Nat. Commun.* **2021**, *12*, 2597. [CrossRef] [PubMed]
7. Becker, P. Borate materials in nonlinear optics. *Adv. Mater.* **1998**, *10*, 979–992. [CrossRef]
8. Mutailipu, M.; Poeppelmeier, K.R.; Pan, S.L. Borates: A rich source for optical materials. *Chem. Rev.* **2021**, *121*, 1130–1202. [CrossRef]
9. Guo, J.R.; Huang, X.; Chen, Q.; Luo, L.; Luo, Y.; Xiong, Y.; Zhang, S. Pechini sol-gel synthesis of $La_2CaB_8O_{16}$: Eu^{3+} red phosphor and its photoluminescence spectral properties. *J. Lumin.* **2019**, *206*, 15–20. [CrossRef]
10. Hermus, M.; Phan, P.C.; Duke, A.C.; Brgoch, J. Tunable optical properties and increased thermal quenching in the blue-emitting phosphor series: $Ba_2(Y_{1-x}\ Lu_x)_5B_5O_{17}$: Ce^{3+} (x = 0–1). *Chem. Mater.* **2017**, *29*, 5267–5275. [CrossRef]
11. Yang, L.; Wan, Y.; Huang, Y.; Chen, C.; Seo, H.J. Development of $YK_3B_6O_{12}$: RE (RE = Eu^{3+}, Tb^{3+}, Ce^{3+}) tricolor phosphors under near-UV light excitation. *J. Alloy. Comp.* **2016**, *684*, 40–46. [CrossRef]
12. Cao, M.; Tian, J.H.; Zhuang, W.D.; Liu, R.H.; Liu, Y.H.; Chen, G.T.; Zhou, G.G.; Wang, L.M.; Wang, J.W. Multisite Cation Regulation of Broadband Cyan-Emitting $(Ba_{1-x}Sr_x)_9Lu_2Si_6O_{24}$:$Eu^{2+}$ Phosphors for Full-Spectrum wLEDs. *Inorg. Chem.* **2022**, *61*, 1805–1815. [CrossRef] [PubMed]
13. Wei, Y.; Gao, Z.Y.; Yun, X.H.; Yang, H.; Liu, Y.X.; Li, G.G. Abnormal Bi^{3+}-activated NIR emission in highly symmetric $XAl_{12}O_{19}$ (X = Ba, Sr, Ca) by selective sites occupation. *Chem. Mater.* **2020**, *32*, 8747–8753. [CrossRef]
14. Du, F.; Zhuang, W.D.; Liu, R.H.; Zhong, J.Y.; Liu, Y.H.; Hu, Y.S.; Gao, W.; Zhang, X.; Chen, L.; Lin, K. Site occupancy and photoluminescence tuning of $La_3Si_{6-x}Al_xN_{11-x/3}$: Ce^{3+} phosphors for high power white light-emitting diodes. *CrystEngComm* **2017**, *19*, 2836–2843. [CrossRef]
15. Bubnova, R.S.; Povolotskiy, A.V.; Biryukov, Y.P.; Kolesnikov, I.E.; Volkov, S.N.; Filatov, S.K. Cation sites occupation and luminescence of novel red-emitting phosphors $Ba_6(Lu_{1-x}Eu_x)_5B_9O_{27}$ (x = 0.02–0.2). *Ceram. Int.* **2022**, *48*, 15966–15974. [CrossRef]
16. Tian, J.; Xie, J.; Zhuang, W. Recent Advances in Multi-Site Luminescent Materials: Design, Identification and Regulation. *Materials* **2023**, *16*, 2179. [CrossRef]
17. Shablinskii, A.P.; Kolesnikov, I.E.; Bubnova, R.S.; Povolotskiy, A.V.; Lähderantac, E.; Filatov, S.K. A novel thermally stable $Ba_3Bi_2(BO_3)_4$:Eu^{3+} red phosphor for solid state lighting application. *J. Lumin.* **2019**, *216*, 116714. [CrossRef]
18. Shablinskii, A.P.; Povolotskiy, A.V.; Kolesnikov, I.E.; Biryukov, Y.P.; Bubnova, R.S.; Avdontceva, M.S.; Demina, S.V.; Filatov, S.K. Novel red-emitting color-tunable phosphors $BaBi_{2-x}Eu_xB_2O_7$ (x = 0–0.40): Study of the crystal structure and luminescence. *J. Solid State Chem.* **2022**, *307*, 122837. [CrossRef]
19. Kolesnikov, I.E.; Bubnova, R.S.; Povolotskiy, A.V.; Biryukov, Y.P.; Povolotckaia, A.V.; Shorets, O.Y.; Filatov, S.K. Europium-activated phosphor $Ba_3Lu_2B_6O_{15}$: Influence of isomorphic substitution on photoluminescence properties. *Ceram. Int.* **2021**, *47*, 8030–8034. [CrossRef]
20. Wang, G.F.; Huang, Q.Z.; Liang, J.K. Studies on phase equilibrium relation in binary section BaB_2O_4-SrB_2O_4 and BaB_2O_4-SrO. *Acta Chim. Sin.* **1984**, *42*, 503–508.
21. Huang, Q.; Huang, L.; Dai, G.; Liang, J. Structure of $Sr_xBa_{3-x}(B_3O_6)_2$ in a Solid Solution. *Acta Crystallogr.* **1992**, *C48*, 539–541. [CrossRef]
22. Sun, T.Q.; Pan, F.; Wang, X.Q.; Shen, G.Q.; Shen, D.Z. Growth, structure and properties of barium strontium borate ($Ba_{0.87}Sr_{3.13}B_{14}O_{25}$) crystal. *Rengong Jingti Xuebao* **2004**, *33*, 935–939.
23. Volkov, S.N.; Bubnova, R.S.; Povolotskiy, A.V.; Ugolkov, V.L.; Arsent'ev, M.Y. Two novel centrosymmetric barium strontium borates with a deep-UV cut-off edge: $Ba_2Sr_3B_4O_{11}$ and $Ba_3Sr_3B_4O_{12}$. *J. Solid State Chem.* **2020**, *281*, 121023. [CrossRef]
24. Furmanova, N.G.; Maksimov, B.A.; Molchanov, V.N.; Kokh, A.E.; Kononova, N.G.; Fedorov, P.P. Crystal structure of the novel barium borate $Ba_5(BO_3)_2(B_2O_5)$. *Crystallogr. Rep.* **2006**, *51*, 219–224. [CrossRef]
25. Bekker, T.B.; Rashchenko, S.V.; Seryotkin, Y.V.; Kokh, A.E.; Davydov, A.V.; Fedorov, P.P. BaO-B_2O_3 system and its mysterious member $Ba_3B_2O_6$. *J. Am. Ceram.* **2018**, *101*, 450–457. [CrossRef]
26. Rashchenko, S.V.; Bekker, T.B.; Bakakin, V.V.; Seryotkin, Y.V.; Simonova, E.A.; Goryainov, S.V. New fluoride borate with 'anti-zeolite' structure: A possible link to $Ba_3(BO_3)_2$. *J. Alloys Compd.* **2017**, *694*, 1196–1200. [CrossRef]
27. Solntsev, V.P.; Bekker, T.B.; Davydov, A.V.; Yelisseyev, A.P.; Rashchenko, S.V.; Kokh, A.E.; Grigorieva, V.D.; Park, S.-H. Optical and Magnetic Properties of Cu-Containing Borates with "Antizeolite" Structure. *J. Phys. Chem. C* **2019**, *123*, 4469–4474. [CrossRef]
28. Bekker, T.B.; Rashchenko, S.V.; Solntsev, V.P.; Yelisseyev, A.P.; Kragzhda, A.A.; Bakakin, V.V.; Seryotkin, Y.V.; Kokh, A.E.; Kokh, K.A.; Kuznetsov, A.B. Growth and Optical Properties of $Li_xNa_{1-x}Ba_{12}(BO_3)_7F_4$ Fluoride Borates with "Antizeolite" Structure. *Inorg. Chem.* **2017**, *56*, 5411–5419. [CrossRef]
29. Bekker, T.B.; Solntsev, V.P.; Rashchenko, S.V.; Yelisseyev, A.P.; Davydov, A.V.; Kragzhda, A.A.; Kokh, A.E.; Kuznetsov, A.B.; Park, S. Nature of the Color of Borates with "Anti-Zeolite" Structure. *Inorg. Chem.* **2018**, *57*, 2744–2751. [CrossRef]
30. Simonova, E.A.; Kuznetsov, A.B.; Svetlichnyi, V.A.; Kononova, N.G.; Shevchenko, V.S.; Nigmatulina, E.N.; Kolesnichenko, M.V.; Kokh, K.A.; Rashchenko, S.V.; Kokh, A.E. Nd^{3+} and Pr^{3+} doped anti-zeolite matrix-$LiBa_{12}(BO_3)_7F_4$: Crystal structures, luminescence properties. *Mater. Chem. Phys.* **2020**, *247*, 122612. [CrossRef]
31. Petříček, V.; Dusek, M.; Palatinus, L. Crystallographic computing system JANA2006: General features. *Z. Kristallogr.* **2014**, *229*, 345–352. [CrossRef]
32. Shannon, R.D. Revised effective ionic radii and systematic studies of interatomic. *Acta Crystallogr.* **1976**, *A32*, 751–767. [CrossRef]
33. Bakakin, V.V. On a dual function of anions in crystallogenesis of compounds: Structure-directing and stabilizing. *J. Struct. Chem.* **2017**, *58*, 947–952. [CrossRef]
34. Rashchenko, S.V.; Bekker, T.B. Crystal chemistry of novel "antizeolite" structures. *J. Struct. Chem.* **2021**, *62*, 1935–1945. [CrossRef]

35. Ilyukhin, A.B.; Dzhurinskii, B.F. Crystal structures of $Ln_{14}(GeO_4)_2(BO_3)_6O_8$ (*Ln* = Nd, Sm) and $Tb(^{3+})_{54}Tb(^{4+})(GeO_4)_{12}O_{59}$. *Zhurnal Neorganicheskoi Khimii* **1994**, *39*, 556–563. (In Russian)
36. Ma, R.R.; Yang, Y.; Hu, C.; Yang, Z.H.; Pan, S.L. The First Examples of Lithium Containing Mixed-Alkali Strontium Borates with Different Dimensional Anionic Architectures and Short Cutoff Edges. *Chem. Eur. J.* **2018**, *24*, 15355. [CrossRef] [PubMed]
37. Filatov, S.K.; Biryukov, Y.P.; Bubnova, R.S.; Shablinskii, A.P. The novel borate $Lu_5Ba_6B_9O_{27}$ with a new structure type: Synthesis, disordered crystal structure and negative linear thermal expansion. *Acta Cryst.* **2019**, *B75*, 697–703.
38. Song, J.L.; Hu, C.L.; Xu, X.; Kong, F.; Mao, J.G. A facile synthetic route to a new SHG material with two types of parallel π-conjugated planar triangular units. *Angew. Chem. Int. Ed.* **2015**, *54*, 3679. [CrossRef]
39. Niu, X.; Wang, L. Synthesis, characterization and crystal structure of a new mixed alkali and alkaline-earth metal borate $Rb_9Ba_{24}(BO_3)_{19}$. *New J. Chem.* **2020**, *44*, 3882–3887. [CrossRef]
40. Biryukov, Y.P.; Bubnova, R.S.; Krzhizhanovskaya, M.G.; Filatov, S.K.; Povolotskiy, A.V.; Ugolkov, V.L. Thermal behavior of polymorphic modifications of $LuBO_3$. *Solid State Sci.* **2020**, *99*, 106061. [CrossRef]